





Spectral proxies for bonding transitions in SiO₂ and MgSiO₃ polymorphs at high pressure up to 270 GPa by O *K*-edge x-ray Raman scattering

Yoo Soo Yi ^{1,2}, Hoon Khim,¹ Yong-Hyun Kim ¹ and Sung Keun Lee ^{1,3,*}

¹Laboratory of Physics and Chemistry of Earth Materials, School of Earth and Environmental Sciences, Seoul National University, Seoul 08826, Korea

²Korea Polar Research Institute, Incheon 21990, Korea

³Institute of Applied Physics, Seoul National University, Seoul 08826, Korea

 (Received 2 April 2021; revised 2 June 2021; accepted 3 June 2021; published 17 June 2021)

Advances in synchrotron x-ray Raman scattering (XRS) techniques enable probing of pressure-induced element-specific bonding transitions in diverse oxides beyond megabar pressures. Evolution of the electronic structures under extreme pressure involves an emergence of additional oxygen 1s electron excitation pattern and shifts in the electronic states toward high-energy ranges in an XRS spectrum. Structural origins of such changes and proper spectral proxy for the corresponding evolution in electronic density of states remain to be established. Here, we calculated the O *K*-edge features in the XRS spectrum for diverse crystalline SiO₂ polymorphs, from α -quartz (1 atm) to a pyrite-type structure (at ~ 271 GPa), beyond the current experimental pressure limit (~ 160 GPa). The *ab initio* results unravel the electronic origins of the evolution in the XRS patterns, such as the emergence of the bimodal feature with decreasing oxygen-oxygen distance ($d_{\text{O-O}}$) $< \sim 2.5$ Å and a subsequent merging of the doublet patterns with a further decrease in $d_{\text{O-O}}$ down to ~ 2.3 – 2.4 Å. *Ab initio* simulations of the XRS spectrum of pyrite-type SiO₂ phase at ~ 271 GPa revealed the significant electron dispersion in $2p^*$ states and the pronounced electron density between edge-sharing oxygen atoms with $d_{\text{O-O}}$ of ~ 2.1 Å, in contrast to an earlier prediction with a negligible electron density between those oxygen atoms. The pressure-induced increase in electron interactions leads to a systematic change in the edge energy at half of the spectrum area (E_M) and the edge energy at the center of mass of the spectrum (E_C) of XRS patterns beyond multimegabar pressures. Particularly, the E_M and E_C increase linearly with decreasing oxygen proximity ($d_{\text{O-O}}$) and bulk density up to 270 GPa. The E_M and E_C for MgSiO₃ phases show larger changes with varying $d_{\text{O-O}}$ than those in SiO₂ phases, demonstrating the effect of the electronic hybridization between Mg and O on the evolution of the XRS patterns. The strong linear correlation among E_M , E_C , and $d_{\text{O-O}}$ (and density) up to ~ 270 GPa confirms that the E_M and E_C can be effective spectral proxies to quantify the densification of crystalline and noncrystalline oxides. The results with the statistical evaluations of the electronic density of states provide improved prospects for the prediction of the evolution in core-level excitation features of diverse complex, multicomponent oxides under multimegabar pressure conditions toward the deep lower mantle of Earth and other super-Earth bodies.

DOI: [10.1103/PhysRevB.103.214109](https://doi.org/10.1103/PhysRevB.103.214109)

I. INTRODUCTION

The pressure-induced changes in the atomic and the electronic structures of prototypical oxides, such as SiO₂ phases under extreme compression, allow us to infer their densification mechanisms at high pressures [1–3]. They also provide useful constraints on the densification of more complex crystalline and amorphous silicates, such as melts and glasses in Earth's interior, where the potential for the presence of SiO₂ high-pressure polymorphs [4–6] and high-density SiO₂-rich silicate melts [7–9] has been proposed. Crystalline SiO₂ undergoes phase transitions from α -quartz to coesite at ~ 2 – 3 GPa [10], to stishovite at ~ 8 – 9 GPa [11], to CaCl₂-type SiO₂ at ~ 47 – 55 GPa [12–16], and to α -PbO₂-type SiO₂ at ~ 98 – 121 GPa [6,13,15,16]. These phase transitions have been proposed as an origin of local seismic

discontinuities in Earth's interior [4–6,9,12–17]. With additional increase in pressure, it transforms to pyrite-type SiO₂ at ~ 226 – 268 GPa [4,5,13,17] and to hexagonal Fe₂P-type SiO₂ $> \sim 640$ GPa [18], which may provide insights into the structural transitions in the silicate mantles of super-Earth bodies.

Direct probing of the bonding nature and electronic structures of SiO₂ phases is therefore essential to account for the nature of phase transitions upon densification in Earth and planetary interiors. Synchrotron x-ray Raman scattering (XRS, also known as nonresonant inelastic x-ray scattering) is the only experimental technique that directly probes element-specific electronic structures and chemical bonding around low-*z* elements at elevated pressure conditions [19–25]. Particularly, O *K*-edge XRS unveiled pressure-induced changes in the local structures and topologies around oxygen atoms for various oxide crystals and primarily for oxide glasses under compression ([19,20,26–37] and references therein). As the main goal of this paper is to establish suitable spectral

*Corresponding author: sungklee@snu.ac.kr

proxies for the oxide densification based on O *K*-edge XRS, a summary of the progress in both experiments and theoretical calculations is briefly discussed here. Because the XRS technique is effective in resolving electronic structures for amorphous oxides, we note that the main experimental progress has been made for noncrystalline oxides. Here, these previous XRS studies are presented in chronological order. Lee *et al.* [38] reported high-pressure measurements of O *K*-edge XRS signals for oxide glasses (B_2O_3) at 8 GPa (along with B *K*-edge XRS signal up to 23 GPa), revealing the prevalence of tetra-coordinated boron. Lin *et al.* [39] reported the changes in O *K*-edge XRS patterns of SiO_2 glass up to ~ 51 GPa, suggesting a bonding transition that occurs from an increase in Si coordination numbers from $^{[4]}Si$ to $^{[6]}Si$. Lee *et al.* [31] probed the local electronic structures of $MgSiO_3$ glasses under high pressures up to ~ 39 GPa using oxygen *K*-edge XRS. XRS spectra for shock-compressed quaternary silicate glass on a diopside-anorthite eutectic composition with a peak pressure of ~ 20 GPa was used to account for the shock-induced densification in glass networks [40]. Lelong *et al.* [35] reported the O *K*-edge XRS for GeO_2 glass up to ~ 18 GPa. Reviews of such progress are summarized by Lee *et al.* [20] and Sternemann and Wilke [26]. An O *K*-edge XRS study by Moulton *et al.* [41] explored the pressure-induced structural evolution of diopside ($CaMgSi_2O_6$) glass up to ~ 20 GPa. Through oxygen *K*-edge XRS, Hiraoka *et al.* [42] reported extended x-ray absorption fine-structure spectra for $MgSiO_3$ glass up to ~ 30 GPa.

The experimental breakthroughs of XRS experiments involving the postcollimation of scattered x rays [43] allow XRS signals for simple oxide glasses at high pressures > 100 GPa to be collected [29,30,36]. Lee *et al.* [36] reported megabar XRS spectra for prototypical B_2O_3 glass at high pressure up to ~ 121 GPa and suggested the densification model based on O-O distance reduction. Petitgirard *et al.* [37] reported the detailed O *K*-edge XRS spectra of archetypal amorphous SiO_2 up to ~ 108 GPa with experimental breakthroughs involving thin diamond anvils. Lee *et al.* [29] also reported the pressure-induced changes in O *K*-edge features of SiO_2 glass up to ~ 160 GPa, which is the current high-pressure limit of the XRS study. Kim *et al.* [30] reported the O *K*-edge spectra for $MgSiO_3$ glasses up to ~ 130 GPa, yielding insights into dense magmatic melts at the bottom of the lower mantle, comprising the ultralow velocity zone.

While the above progress enables collection of the pressure-induced changes in XRS spectra of diverse oxides up to 160 GPa, interpretation of the XRS spectrum is not trivial because the overlaps among the core electron excitation patterns for diverse structurally distinct atomic environments (i.e., crystallographically distinct sites and/or those from glassy networks) become prevalent at higher-pressure conditions [20]. Understanding the correlation between the changes in oxygen-specific environments and the corresponding XRS patterns upon compression requires inputs from *ab initio* calculations [44]. Indeed, *ab initio* calculations for low-*z* elements in oxides and silicates at high pressures have been successful in reproducing the experimental XRS through unoccupied partial density of states (PDOS) [20,27,37,45–48], accounting for the O and B *K*-edge and Si $L_{2,3}$ -edge XRS spectra of $MgSiO_3$, B_2O_3 , and SiO_2 high-pressure

phases upon phase transition [27–30,47,48]; for example, Lin *et al.* [39] calculated the O *K*-edge XRS spectrum for stishovite. Fukui *et al.* [47] reported calculated oxygen PDOS of various SiO_2 polymorphs at high-pressure. Yi and Lee [28] introduced the concept of XRS crystallography in which the site-resolved calculations for crystallographically distinct atoms are provided. The results showed the evolution in XRS patterns for various SiO_2 and $MgSiO_3$ upon phase transitions. Based on the *ab initio* simulations, the O *K*-edge XRS pattern at ~ 544 eV for $MgSiO_3$ glass $> \sim 20$ GPa [31] was attributed to densification via reduced distance between oxygen atoms. Wu *et al.* [49] calculated O *K*-edge XRS spectra for compressed amorphous SiO_2 , revealing electronic origins of densification in the glass (see Sec. 1 of the Supplemental Material (SM) [50]; see, also, references [29–31,39,49] therein). Based on *ab initio* simulations of the O *K*-edge XRS spectra for crystalline $MgSiO_3$ polymorphs, Yi and Lee [27] explored a relationship between the evolution in XRS patterns (parameterized with E_A , that is, the edge energy at which the main XRS feature starts to increase) and the average O-O distances, suggesting that E_A of the XRS pattern can explain the densification of such oxides (i.e., the E_A method). The E_A method has then been used in recent studies of oxide crystals and glasses [29,30,36,37]. In recent studies of SiO_2 glasses at high pressure, the emergence of high-energy features in O *K*-edge XRS spectra of high-density SiO_2 glasses has been attributed to how the arrangements of Si and oxygen atoms vary under compression based on the calculated O *K*-edge XRS features of crystalline SiO_2 [29]; the high-energy feature at ~ 548 eV was suggested to be due to changes in glass networks accompanied with the formation of oxygen quadcluster ($^{[4]}O$) and a decrease in oxygen proximity. Despite these efforts and experimental advances, the atomistic interpretation of characteristic O *K*-edge excitation patterns of SiO_2 phases above megabar pressures remains to be explored further. Theoretical confirmations have been anticipated for high-pressure silicate crystals beyond multimegabar pressures up to ~ 270 GPa, which is relevant to the deep mantles of super-Earth bodies.

These experimental and theoretical results help us to establish the spectral proxy in XRS to account for the detailed electronic origins of densification. For example, the increases in E_A and band gap (E_G) of the SiO_2 and $MgSiO_3$ high-pressure phases have been among the useful proxies for oxide densification [27]. While the changes in E_A upon compression describe the pressure-induced changes in densification in oxides and silicates, its application can be somewhat complicated, primarily because of the emergence of high-energy peaks in PDOS from the contracted oxygen environments and the peak broadening due to electronic delocalization [29]. Because E_A represents only the shifting of the XRS spectrum with the edge onset value, it cannot fully quantify such complicated changes in the spectral variations upon compression. In our recent study, we showed that the center of gravity of the XRS features (E_C) for crystalline and amorphous SiO_2 at high pressure can account for the spectral evolution during compression [29]. Despite this progress, the utility of those proposed spectral proxies needs to be evaluated, particularly at higher-pressure conditions. The electronic structures and XRS patterns caused by these heavily contracted oxygen

environments beyond the current experimental limit (160 GPa) have yet to be probed. Adding XRS results for the SiO₂ phase far beyond ~ 160 GPa, together with the quantitative evaluation of the spectral proxies may allow us to constrain the structural origin of the changes in electronic structures upon densification more effectively.

To complement our previous studies of the atomistic-level origins of such high-energy features and XRS-based spectral proxies [27–30], we conducted the calculations of the XRS spectra for SiO₂ high-pressure phases from the α -quartz (at 1 atm) to the pyrite-type structure (at 271 GPa) beyond current experimental limitations. Specifically, we calculated the site-resolved O *K*-edge XRS spectra for SiO₂ polymorphs with varying pressures beyond 2 megabar pressures. Using the current theoretical results and those in previous experimental studies for MgSiO₃ phases [27,28], we compared several oxygen-site specific spectral proxies for oxide densification based on XRS under extreme compression. The pressure-induced changes in E_A , E_C , and the median of the spectrum (E_M ; the edge energy at half of the spectrum area) are calculated to assess structural densification in oxides through oxygen *K*-edge XRS above multimegabar pressure conditions. The comprehensive investigation of the XRS-based spectral proxies provides insights into the element-specific structural densification in oxides under extreme compression.

II. CALCULATIONS

A. Crystal structures

Crystal structures of SiO₂ polymorphs [Si coordination environments, lattice parameters, average Si-O bond length ($d_{\text{Si-O}}$), average O-O distance ($d_{\text{O-O}}$), and average Si-O-Si bond angle] are summarized in Table I. The SiO₂ phases studied here include α -quartz (⁴Si; ~ 1 atm) [51], β -quartz (⁴Si; ~ 1 atm) [52], α -cristobalite (⁴Si; ~ 1 atm) [53], coesite (⁴Si; ~ 3.8 GPa) [10], hp-cristobalite (⁴Si; ~ 20 GPa) [54], penta-SiO₂ (⁵Si; ~ 16 GPa) [55], stishovite (⁶Si; ~ 9.3 and ~ 29.1 GPa) [11], a CaCl₂-type structure (⁶Si; ~ 63 GPa) [56], an α -PbO₂-type structure (⁶Si; ~ 120 GPa) [57], and a pyrite-type structure (⁶Si; ~ 271 GPa) [17] (Fig. 1, visualized with VESTA [58]). Quartz (α and β) and cristobalite (α and hp) exhibit the corner-sharing topologies that connect crystallographically identical four-coordinated Si atoms (⁴Si-O-⁴Si). The coesite consists of Si and O atoms with crystallographically distinct atomic sites, where the O atoms exhibit corner-sharing topologies connecting either crystallographically identical or distinct Si atoms (⁴Si#-²O#-⁴Si#, # = 1, 2 or ⁴Si1-²O#-⁴Si2, # = 3, 4, 5). The penta-SiO₂ structure consists of crystallographically distinct O atoms, connecting SiO₅ polyhedra (⁵Si-³O1-2⁵Si and ⁵Si-²O2-⁵Si, respectively). The edge-sharing O atom in the penta-SiO₂ structure (⁵Si-³O1-2⁵Si) is triply coordinated by the surrounding Si atoms, forming an oxygen tricluster (³O). The stishovite and the CaCl₂-type structure, which consist of SiO₆ octahedra, exhibit edge- and corner-sharing topologies. The O atoms in SiO₂ polymorphs with SiO₆ polyhedra are triply coordinated by ⁶Si (⁶Si-³O-2⁶Si). The α -PbO₂-type structure shows the dense packing of SiO₆ octahedra relative to the stishovite and the CaCl₂-type structure, but the

topologies for SiO₆ octahedra remain identical (e.g., corner- and edge-sharing topologies; ⁶Si-³O-2⁶Si). The pyrite-type structure presents corner-sharing topologies connecting SiO₆ octahedra in contrast to the stishovite, CaCl₂-type, and α -PbO₂-type structures, while the O atoms are triply coordinated with ⁶Si atoms (see aforementioned references for further details).

B. Electronic structures and O *K*-edge XRS spectra

The local electronic structures and O *K*-edge XRS spectra of SiO₂ phases were calculated using *ab initio* calculations based on the full-potential linearized augmented plane wave with local orbitals method (WIEN2k) [59]. Electronic structure calculations were carried out without further structural optimization. The Perdew-Burke-Ernzerhof exchange-correlation functional optimized for solids was applied to describe the onsite electron-electron interactions [60]. The muffin-tin radii of Si and O atoms were set to 1.34–1.64 and 1.45–1.64 Å. The energies for core-valence separation were set to -7.2 to -6.0 Ry (1 Ry = 13.6 eV). The numbers of *k* points in the irreducible Brillouin zone were set to 24–48 [35,45,47]. The convergence criteria of self-consistent field calculations were set to 1×10^{-4} Ry and 1×10^{-4} e for the total energy and charge distance, respectively. The details of the parameters are further discussed in our previous studies [27,28] and other references [45,61].

During the XRS, incident x-ray photons cause the electronic transitions of core electrons to the unoccupied states [19]. The empty core states remained after the transitions affect the local electronic structures, particularly for the low-*z* elements [45]. These core-hole effects should be considered to fully reproduce the O *K*-edge XRS features for SiO₂ polymorphs. The sizes of the extended supercell structures, used to reduce the interactions between core-holes, are presented in Table I; the convergence of the O *K*-edge spectra with the size of the supercell was achieved (see Sec. 3 of the SM [50]; see also Refs. [27,28,31,39,45,62] therein), successfully reproducing experimental XRS spectra for crystalline SiO₂ and Mg silicates [27,28]. Practical aspects of applying the core-hole effects are well summarized in previous studies [27,28,45]. The core-level XRS features presented here are determined from the double differential scattering cross-section under dipole-allowed transitions as well as monopole and other higher-order terms, which describe the electron energy transfer due to inelastic scattering in electron energy loss spectroscopy (EELS) [45,59]. The features are identical to those of the electron-loss near-edge structure (ELNES) obtained from the XRS experiments in the low-*q* limit [19,45]. In our earlier XRS experiments, we have collected the various *K*-edge XRS spectra for diverse low-*z* oxide with varying scattering angles from 18° ($q = 1.74 \text{ \AA}^{-1}$) to 75° ($q = 6.11 \text{ \AA}^{-1}$) (see Refs. [20,36] and references therein). These studies do not reveal noticeable change in the XRS spectra due to changes in scattering angle (and thus, the magnitude of scattering vector), while the changes in Compton peaks near elastic peak are prevalent up to energy loss of ~ 150 eV at a large scattering angle of 75°. These studies confirm that similar oxide crystals (silica and silicates) investigated in this paper are not expected to show a noticeable *q* dependence.

TABLE I. Si coordination environments, space groups, lattice parameters, pressure conditions, and interatomic distances of crystalline SiO₂ polymorphs.

Phase	^[4] Si			^[5] Si			^[6] Si			
	α -quartz ^a	β -quartz ^b	α -cristobalite ^c	Coesite ^d	hp-cristobalite ^e	Penta-SiO ₂ ^f	Stishovite ^g	CaCl ₂ -type SiO ₂ ^h	α -PbO ₂ -type SiO ₂ ⁱ	Pyrite-type SiO ₂ ^j
System	Trigonal	Hexagonal	Tetragonal	Monoclinic	Tetragonal	Trigonal	Tetragonal	Orthorhombic	Orthorhombic	Cubic
Space group	(¹⁵²)P3 ₁ 21	(¹⁸⁰)P6 ₂ 22	(⁹²)P4 ₁ 2 ₁ 2	(¹⁵)C2/c	(⁹²)P4 ₁ 2 ₁ 2	(¹⁵⁴)P3 ₂ 21	(¹³⁶)P4 ₂ /mnm	(⁵⁸)Pnmm	(⁶⁰)Pbcn	(²⁰⁵)Pa $\bar{3}$
Pressure (GPa)	1 atm	1 atm	1 atm	~3.8	~20	~16	~9.3	~29.1	~120	~271
Lattice parameter (Å)										
a	4.912	4.997	4.969	7.020	4.355	4.414	4.134	4.044	3.711	3.923
b	4.912	4.997	4.969	12.262	4.355	4.414	4.134	4.044	4.651	3.923
c	5.404	5.457	6.926	7.126	5.960	9.358	2.654	2.619	4.159	3.923
Average Si-O bond length (Å)	1.608	1.588	1.603	1.605	1.554	1.703	1.760	1.729	1.649	1.605
Average O-O distance (Å)	2.626	2.593	2.618	2.621	2.522	2.561	2.487	2.442	2.327	2.264
Average Si-O-Si bond angle (°)	143.72	153.28	146.38	140.84	135.07	126.90	130.58	130.58	128.39	119.60
				180.00 ^k		97.27 ^k	98.84 ^k	98.84 ^k	97.76 ^k	
Si-O polyhedral volume (Å ³)	2.1339	2.0531	2.1145	2.1202	1.8484	3.9297	7.1856	6.8067	5.9201	5.3380
Density (g/cm ³)	2.65	2.54	2.33	3.03	3.53	3.79	4.40	4.66	5.56	6.61
Supercell sizes	2×2×1	2×2×1	2×2×1	1×1×1	2×2×1	2×1×1	2×2×2	2×2×2	2×1×2	2×1×2
Number of atoms	36	36	48	48	48	36	48	48	48	48
Distance between excited O atoms* (Å) ^l	5.404	5.457	6.926	7.020	5.960	4.414	5.308	5.238	4.651	3.923

^aReference [51]; ^bReference [52]; ^cReference [53]; ^dReference [10]; ^eReference [54]; ^fReference [55]; ^gReference [11]; ^hReference [56]; ⁱReference [57]; ^jReference [17].

^kThese values present distinctive Si-O-Si bond angles in the SiO₂ polymorphs.

^lThe distance between excited oxygen atoms due to the use of periodic boundary condition.

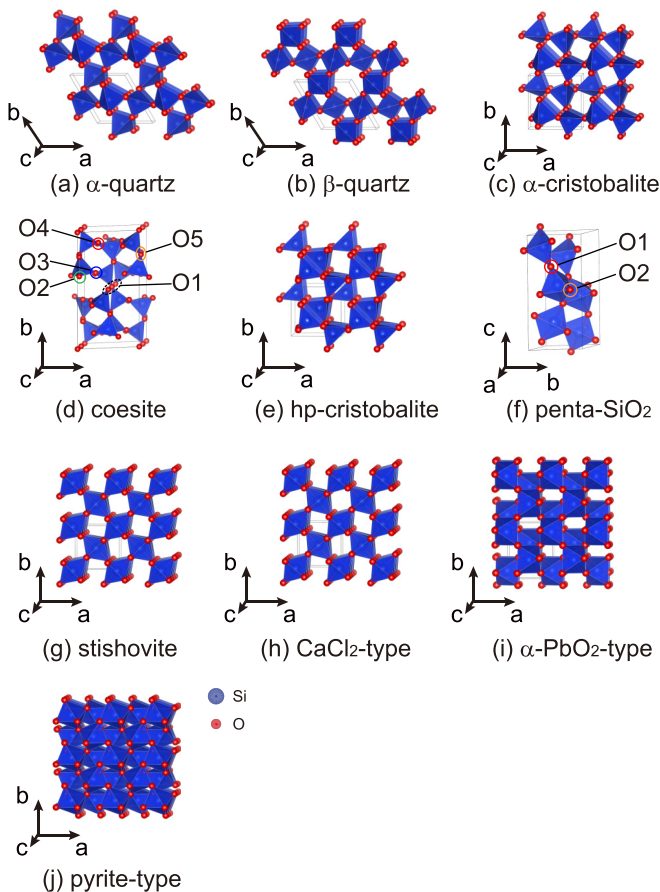


FIG. 1. Crystal structures of (a) α -quartz, (b) β -quartz, (c) α -cristobalite, (d) coesite (O1–O5), (e) hp-cristobalite, (f) penta-SiO₂ (O1 and O2), (g) stishovite, (h) CaCl₂-type, (i) α -PbO₂-type, and (j) pyrite-type structures. Details of crystal structure information are summarized in Table I.

Furthermore, an earlier theoretical study of Li-bearing crystalline oxides (LiBO₂, Li₂CO₃, and Li₂O) showed that their O *K*-edge spectra do not show strong *q* dependence with the magnitude of scattering vector from 2.4–4.5 to 8.5–10.2 Å⁻¹ [63]. Finally, in our high-pressure experiment, the typical scattering angle is $\sim 25^\circ$ ($q = 2.17 \text{ \AA}^{-1}$ and $qr = 0.22$); and in our calculations of O *K*-edge XRS spectra, the magnitude of the *q* vector is 1.06 Å⁻¹ and *qr* is 0.11. Taking these small *qr* values into consideration, the main XRS features are largely explained by the dipole approximation [20]. Nevertheless, the effect of scattering angle on the O *K*-edge XRS features for other metal-bearing oxides at high pressure remains to be explored.

The *l*-resolved PDOS of O atoms in the SiO₂ polymorphs was calculated with the core-hole effect. The O *K*-edge XRS spectra were calculated considering the contributions of crystallographically distinct O atoms; the total O PDOSs and O *K*-edge XRS features for coesite and the penta-SiO₂ structure were obtained from the linear summation of XRS spectra for crystallographically distinct oxygen sites. These calculated PDOSs are presented for unoccupied states above the Fermi level (from 0 to 30 eV) with a broadening factor of 0.003 Ry. The *l*-resolved PDOSs of Si and O atoms calculated without

considering core-hole effects are presented in the SM (Fig. S6) [50]. The calculated O *K*-edge XRS spectra are presented up to 30 eV with a broadening factor of 0.5 eV. The calculated XRS spectra were shifted by 531 eV for SiO₂ phases and 529.5 eV for MgSiO₃ phases to compare with results from the XRS experiments (see details in our previous studies [29,30]).

III. RESULTS AND DISCUSSION

A. Structure-topology-density relationship

Figure 2 presents the relationships among $d_{\text{Si-O}}$, $d_{\text{O-O}}$, and density (ρ) of SiO₂ polymorphs with varying pressures up to ~ 271 GPa; the effect of pressure on $d_{\text{Si-O}}$ and $d_{\text{O-O}}$ is shown in Figs. 2(a) and 2(b). The relationships among the ρ of SiO₂ polymorphs, $d_{\text{Si-O}}$, and $d_{\text{O-O}}$ are also shown [Figs. 2(c) and 2(d)], which reveal that $d_{\text{O-O}}$ decreases linearly with increasing density [$\rho(\text{g/cm}^3) = -10.7 \times d_{\text{O-O}}(\text{\AA}) + 30.6 (R^2 = 0.95)$]. This confirms that $d_{\text{O-O}}$ can be a useful proxy for the densification of SiO₂ polymorphs under high pressures, as can be inferred from the largest volumetric fraction of oxygen in simple dioxides [29]. The densities of the SiO₂ polymorphs with increasing pressures are presented in the SM (see Sec. 2 of the SM and Fig. S1 [50]). The relationships among the density, $d_{\text{Si-O}}$, and Si coordination numbers are shown in Fig. 2(c), but the correlations are weak because the formation of highly coordinated Si upon phase transition is accompanied by an abrupt increase in the $d_{\text{Si-O}}$. Figure 3 presents the partial radial distributions of the O-O and Si-O pairs in the SiO₂ polymorphs and reveals the systematic pressure-induced decrease in $d_{\text{O-O}}$, along with the complex evolution of $d_{\text{Si-O}}$ upon compression and phase transition. This information is central to establishing the topological origins (e.g., $d_{\text{Si-O}}$ and $d_{\text{O-O}}$) of the XRS features at high pressures (see further discussion below).

B. Partial electronic density of states and O *K*-edge XRS spectra for crystalline SiO₂ phases at high pressure

Figure 4 presents the site-resolved O PDOS (i.e., crystallographically distinct oxygen site specific), the momentum (*l*-resolved O PDOS (the unoccupied O *s*, *p*, and *d* states), and the O *K*-edge XRS spectra of coesite and the penta-SiO₂ structure via *ab initio* calculations. Their unoccupied O *p* states in Figs. 4(a) and 4(c) are like the corresponding XRS patterns in Figs. 4(b) and 4(d), indicating that the XRS features stem mainly from the O 1*s*-2*p** transition [19]. The site-resolved XRS spectra of coesite show the quartzlike patterns for all crystallographically inequivalent corner-sharing O sites (O1–O5) that connect SiO₄ tetrahedra (⁴Si–²O–⁴Si) [Fig. 4(b)]. The site-resolved O *K*-edge XRS spectra for the penta-SiO₂ structure in Fig. 4(d) present the bimodal patterns that are characterized by features at ~ 538 and ~ 544 eV for both edge-sharing O1 (⁵Si–³O1–2⁵Si) and corner-sharing O2 (⁵Si–²O2–⁵Si) sites. This bimodal pattern is characteristic of the O *K*-edge XRS spectra of stishovite [Fig. 5(b)]. Note that the structural origins of the bimodal features have been suggested to be the formation of highly coordinated Si atoms (e.g., ^{5,6}Si) [39,49] and/or contraction in the $d_{\text{O-O}}$ within the edge-sharing topology of

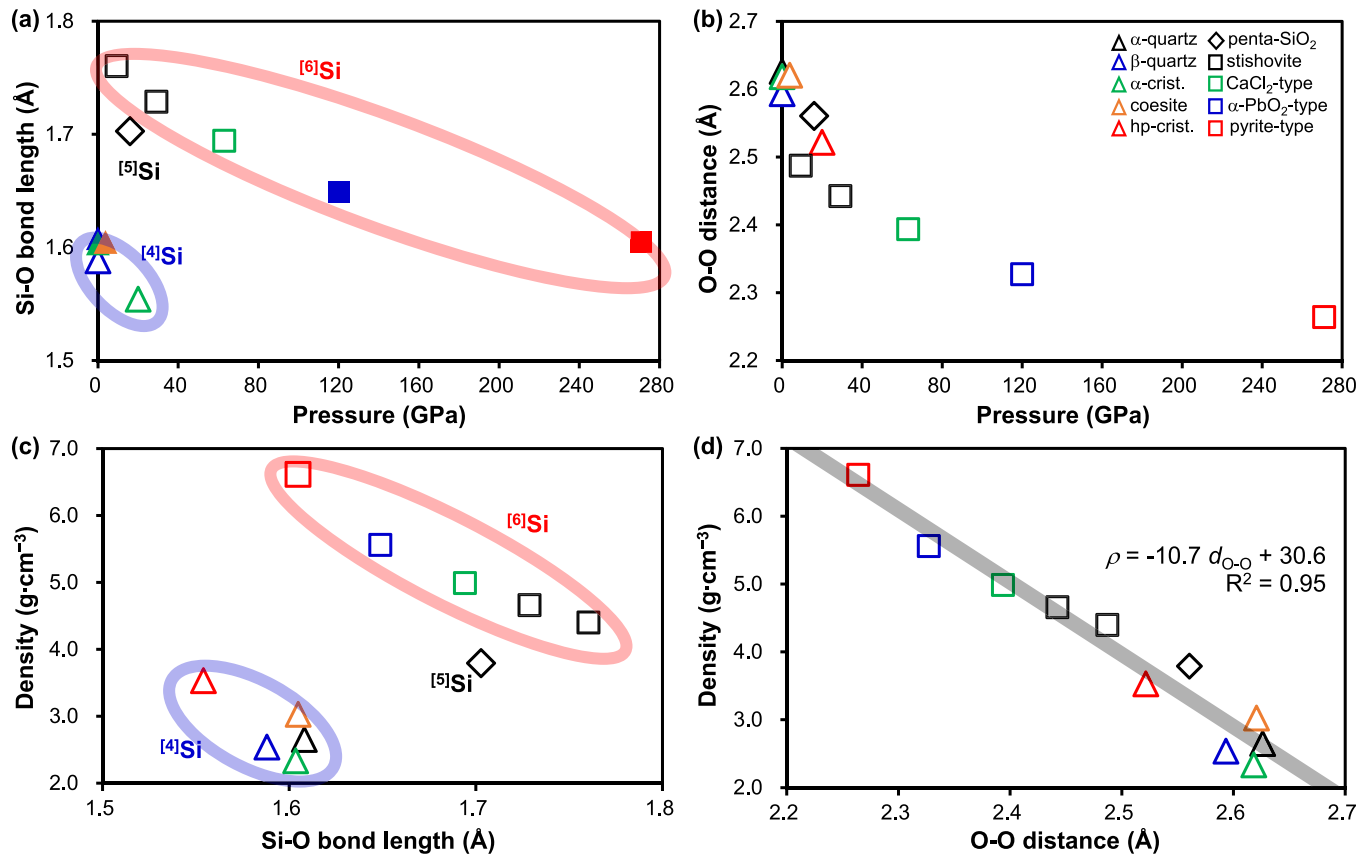


FIG. 2. (a) The average Si-O bond lengths ($d_{\text{Si-O}}$) of the crystalline SiO₂ polymorphs with increasing pressures. (b) The average interatomic distances between nearest-neighboring O atoms ($d_{\text{O-O}}$) with increasing pressures. (c) Relationship between the densities of SiO₂ polymorphs (ρ) and $d_{\text{Si-O}}$. (d) Relationship between ρ and $d_{\text{O-O}}$. The black line shows the linear trend line for the density of SiO₂ polymorphs with varying $d_{\text{O-O}}$.

SiO₆ octahedra [27–29]. However, the current spectra for the penta-SiO₂ structure reveal similar bimodal XRS features for edge-sharing O1 and corner-sharing O2 sites. This indicates that the emergence of the bimodal XRS features may not be controlled by the topologies (edge sharing vs corner sharing) of SiO_x polyhedra. Rather, the peculiar XRS pattern is due primarily to contraction in the $d_{\text{O-O}}$, regardless of Si coordination number (see further discussion below).

Figure 5 shows the l -resolved oxygen-specific density of states and the O K -edge XRS pattern for SiO₂ polymorphs. Here, the core-hole effect was considered (see methods above). The evolution of the O PDOS at conduction bands, which the XRS probes, often involves emergence of high-energy features with substantial delocalization. The distinctive O K -edge XRS features and O PDOS result from the characteristic atomic configuration, symmetry, and topology around oxygen atoms in these SiO₂ phases [27,29]. Similarities between the O K -edge XRS spectrum and their unoccupied oxygen p states again indicate the dominant contributions from the transition of core electron to $2p^*$ in XRS spectra [19]. The electronic delocalization increases with increasing pressures, as demonstrated by the broadening of the occupied s , p , and d states of Si and O atoms (see Sec. 5 of the SM and Fig. S6 [50]).

The distinct XRS patterns for diverse phases exhibit prominent pressure dependence. First, the calculated XRS spectra

for 1 atm and low-pressure phases at 4.3 GPa, such as α -quartz, β -quartz, coesite, and α -cristobalite are similar, showing a main feature at ~ 538.7 eV. This feature can be attributed to the bridging oxygen atoms that connects four-coordinated Si atoms ($^{[4]}\text{Si}$ - $^{[2]}\text{O}$ - $^{[4]}\text{Si}$), where the O PDOS shows the hybridization of O $2p$ states and Si $3s$ and $3p$ states [39].

Second, the calculated XRS spectra for the low- to intermediate-pressure phases, such as hp-cristobalite, the penta-SiO₂ structure, and stishovite (at ~ 9.3 and ~ 29.1 GPa) reveal doublelike O K -edge XRS features at ~ 538 eV (σ^*) and ~ 544 eV (π^*). The XRS feature at ~ 538 eV can be attributed to the hybridization of O $2p$ states with Si $3p$ and partly due to the O p - p interactions, whereas the XRS feature at ~ 544 eV arises mostly from the O p - p hybridization among neighboring oxygen atoms [39,47]. The contribution of O p - p hybridization to the O K -edge XRS patterns has also been reported from the ϵ -phase (O₂)₄ molecular solids, where the π^* peak at ~ 532 eV ($1s$ - $1\pi_g^*$ transition) and the σ^* peak at ~ 540 eV ($1s$ - $3\sigma_u^*$ transition) comprise the bimodal feature at high pressures [24]. Note that hp-cristobalite ($^{[4]}\text{Si}$), the penta-SiO₂ structure ($^{[5]}\text{Si}$), and stishovite ($^{[6]}\text{Si}$) exhibit distinct Si coordination numbers and topologies around oxygen atoms. These crystal structures have the O-O pairs with $d_{\text{O-O}} < \sim 2.5$ Å [see Figs. 2(d) and 3(b) for the $d_{\text{O-O}}$ and the O-O radial distribution functions]. Therefore, the bimodal XRS features for SiO₂

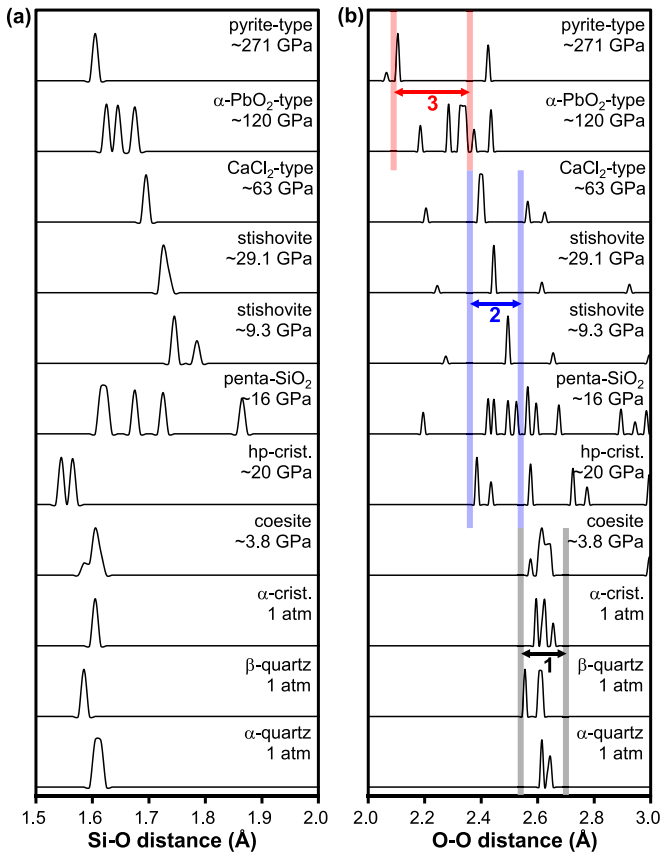


FIG. 3. The partial radial distributions of the Si-O and O-O pairs in the SiO₂ polymorphs (α -quartz, β -quartz, α -cristobalite, coesite, hp-cristobalite, penta-SiO₂, stishovite, CaCl₂-type, α -PbO₂-type, and pyrite-type structures). The d_{O-O} thresholds for characteristic x-ray Raman scattering (XRS) patterns are presented: (1) the α -quartzlike XRS patterns within ~ 2.7 to ~ 2.5 Å, (2) the stishovite-like XRS patterns within ~ 2.5 to ~ 2.4 Å (i.e., the doublet of O p - p hybridization), and (3) the single broad features within ~ 2.4 to ~ 2.1 Å (i.e., the O p - p doublet is apparently merged).

polymorphs at high pressures arise from the enhanced spatial proximity between neighboring O atoms, regardless of the Si coordination environment. Furthermore, the bimodal XRS features in the SiO₂ polymorphs suggest a significant role of p - p hybridization in the electronic bonding structures at high pressures, where the contractions in the d_{O-O} (e.g., $< \sim 2.5$ Å) increase the degree of electronic interactions among the oxygen anions.

Finally, the results for stishovite (~ 9.3 and ~ 29.1 GPa), and other higher-pressure phases, such as the CaCl₂-type structure (~ 63 GPa), and the α -PbO₂-type structure (~ 120 GPa), reveal how the enhanced oxygen proximity affects the O K -edge XRS features for these SiO₂ phases under extreme compression. The characteristic bimodal features of stishovite gradually change with the structural transition to the CaCl₂-type and α -PbO₂-type phases. The bimodal spectral patterns shift to a high energy with a slight broadening (from stishovite to the CaCl₂-type phase). The two peaks merge with increasing pressures, forming a single broad XRS feature for the α -PbO₂-type phase. The observed merging of the bimodal features can be attributed to the contraction in the d_{O-O} further

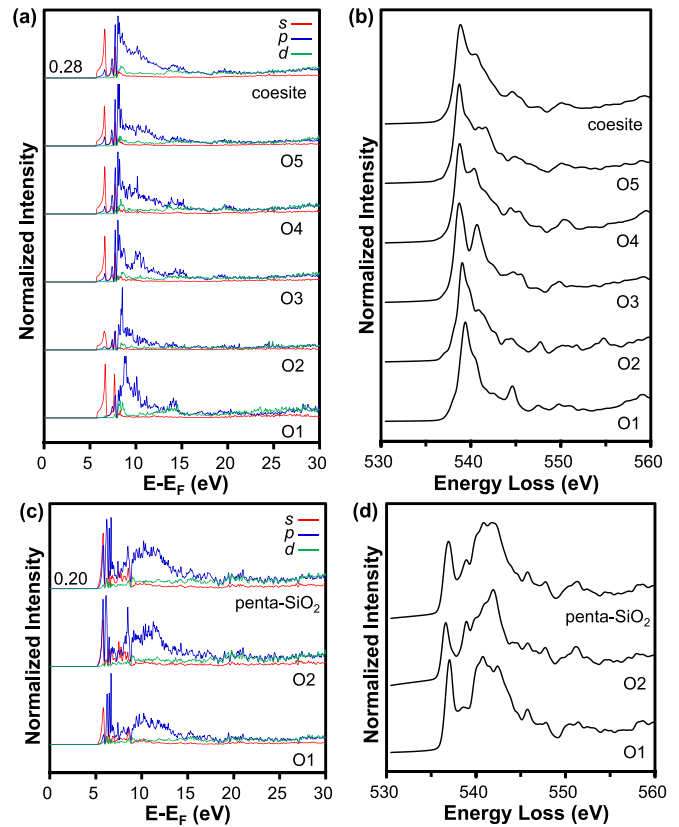


FIG. 4. (a) Site-resolved O partial densities of states (PDOSs) and (b) O K -edge x-ray Raman scattering (XRS) features of coesite (O1–O5). (c) Site-resolved O PDOSs and (d) O K -edge XRS features of penta-SiO₂ structure (O1 and O2). Numbers in the left side of (a) and (c) are the maximum intensity used for the normalization of PDOS.

$< \sim 2.3$ – 2.4 Å and $> \sim 63$ GPa [Figs. 2(d) and 3(b)]. Given the systematic decreases in d_{Si-O} from 1.760 to 1.649 Å and in d_{O-O} from 2.487 to 2.237 Å (Table I and Fig. 3), changes in bimodal peaks at ~ 538 and ~ 544 eV can be attributed to increases in the O p - p hybridization, while decreases in the Si-O bond lengths may also affect the electronic structures at high pressures (see Fig. S6 in the SM [50] for the detailed electronic structures). Note that the stishovite, CaCl₂-type, and α -PbO₂-type structures consist of the edge-sharing SiO₆ octahedra. Therefore, the substantial decreases in the d_{O-O} arise from the structural rearrangements beyond the second coordination shell where the changes in the connectivity of the SiO₆ octahedra contribute to the d_{O-O} contractions upon phase transitions.

C. O K -edge XRS spectrum and electronic structures for the pyrite-type phase at ~ 271 GPa

Pyrite-type SiO₂ exhibits the corner-sharing topology of SiO₆ octahedra with a non-close-packed structure with broad stability fields at high pressures, whereas edge-sharing SiO₆ and/or close packing of oxygen sites are often expected to prevail under extreme compression [64]. A theoretical study proposed that the aspherical electron distributions around the oxygen atoms and the mixed ionic-covalent character of Si-O

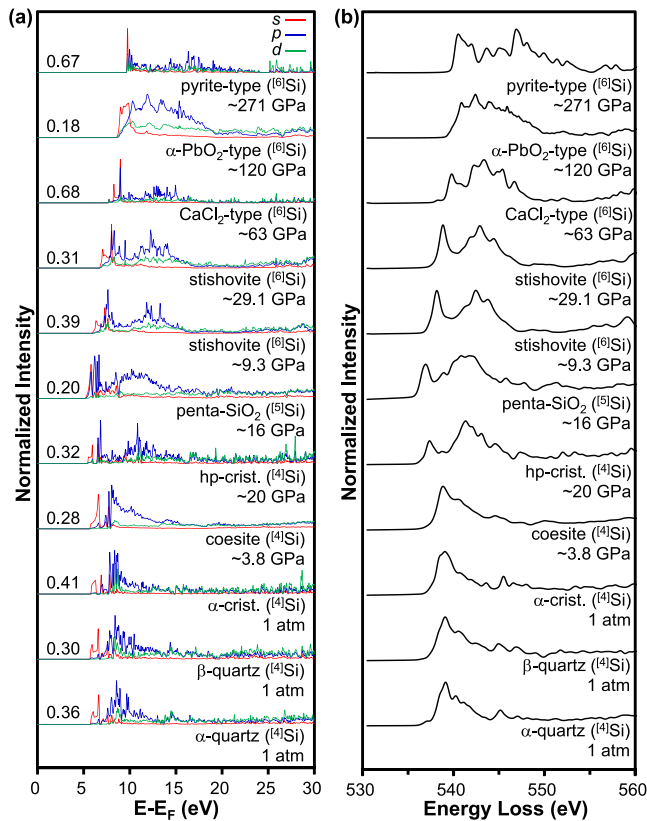


FIG. 5. (a) Calculated l -resolved partial density of states (PDOS) in the unoccupied states of O atoms for SiO_2 polymorphs. The core-hole effects have been considered. Red, blue, and green solid lines refer to the unoccupied O s , p , and d states, respectively. Numbers in the left side of (a) are the maximum intensity used for the normalization of PDOS. (b) Calculated O K -edge x-ray Raman scattering (XRS) features for SiO_2 polymorphs.

bonds may affect the stability of pyrite-type structures at high pressures [64]. In that study, a negligible electron density between O atoms on the (110) plane was observed, indicating that the O p - p interactions were minor in the pyrite-type SiO_2 [64]. This lack of electron densities between oxygen atoms in the pyrite-type phase is in contrast to a significant increase in the O p - p hybridization for SiO_2 polymorphs (e.g., for stishovite, CaCl_2 -type, and α - PbO_2 -type structures) in the calculated PDOS and the XRS spectrum in Fig. 5 and ε -phase solid oxygen atoms at high pressures [24,39]. Furthermore, the O-O distances (~ 2.0 – 2.2 Å) for pyrite-type structures are much shorter than those for stishovite (~ 2.4 – 2.6 Å) (Fig. 3) and solid oxygen atoms (~ 2.34 Å at ~ 11 GPa [65]); therefore, the electronic interactions between neighboring O anions are expected to be substantial.

To reconcile this discrepancy, we explore the electron distribution and interactions between adjacent O atoms in stishovite (at ~ 29.1 GPa) and the pyrite-type structure (at ~ 271 GPa) using *ab initio* calculations based on advance in the exchange-correlation functional and pseudopotential methods. The stishovite results in Fig. 6(a) show noticeable electron densities between neighboring O atoms, sharing the common edge for two SiO_6 octahedra. The electron density map for the pyrite-type phase also reveals the noticeable elec-

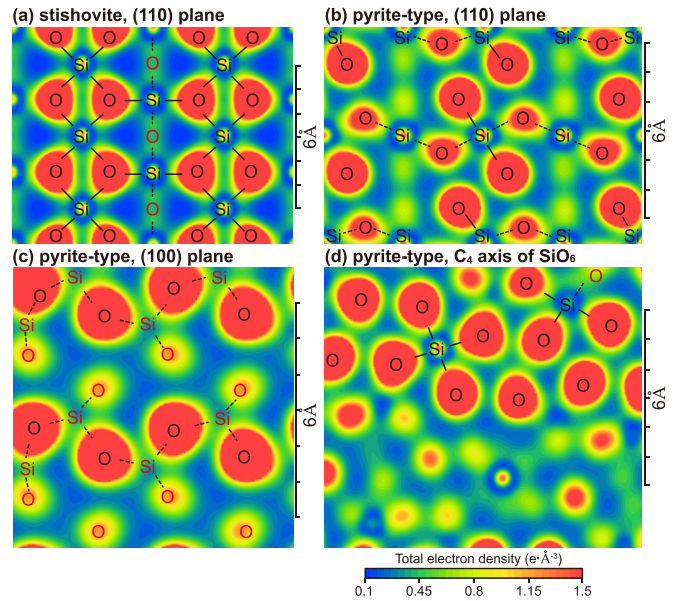


FIG. 6. Total electron densities of the stishovite (at ~ 29.1 GPa) and pyrite-type structure (at ~ 271 GPa), (a) in the (110) plane of stishovite, (b) in the (110) plane of pyrite-type structure, (c) in the (100) plane of pyrite-type structure, and (d) in the plane perpendicular to C_4 symmetry axis of SiO_6 octahedron (including four planar oxygen atoms). Atoms labeled in black and red are those lying or not lying in the given plane, respectively. Solid and dashed lines refer to the Si-O bonds lying or not lying in the given plane, respectively. While the electron densities for stishovite and the pyrite-type structure vary from ~ 0.05 to ~ 7.5 $\text{e} \text{Å}^{-3}$ and from ~ 0.1 to ~ 7.7 $\text{e} \text{Å}^{-3}$, respectively; the projected electron densities are presented from 0.1 to 1.5 $\text{e} \text{Å}^{-3}$ to enhance the visibility of the low electron density distribution between oxygen atoms (see Sec. 6 of the SM for the details of calculation [50]; see also Refs. [75,76] therein).

tron densities between adjacent O atoms in the pyrite-type structure. To further reveal the nature of electron distribution between nearby oxygen atoms, we show the electron density maps projected on several distinct planes {i.e., (110) plane [Fig. 6(b)], (100) plane [Fig. 6(c)], and the plane perpendicular to the C_4 symmetry axis of a SiO_6 octahedron [Fig. 6(d)]}. This allows us to visualize the electron distribution in the pyrite-type phase where the distortion of SiO_6 polyhedra is prevalent. The results confirm the nonnegligible electron distribution between neighboring oxygen atoms.

Extreme densification in the pyrite-type structure reduces the $d_{\text{O-O}}$, which leads to an increase in the degree of O-O electronic interactions and the delocalization of valence electrons (see Sec. 5 of the SM and Fig. S6(k) [50]). The O K -edge XRS spectrum for the pyrite-type phase at ~ 271 GPa in Fig. 5(b) shows the emergence of the additional high-energy feature at ~ 548 eV mainly due to a significant degree of electron delocalization in O $2p^*$ PDOS [Fig. 5(a)]. As also shown in the O-O distance distribution in the pyrite-type phase with a reduced $d_{\text{O-O}} < \sim 2.2$ Å. [Fig. 3(b)], the characteristic XRS pattern with a feature at ~ 548 eV arises from the densification associated with the substantial decreases in the O-O distances.

In noncrystalline SiO_2 , the XRS feature at ~ 548 eV has also been observed for the SiO_2 glasses $> \sim 100$ GPa. The

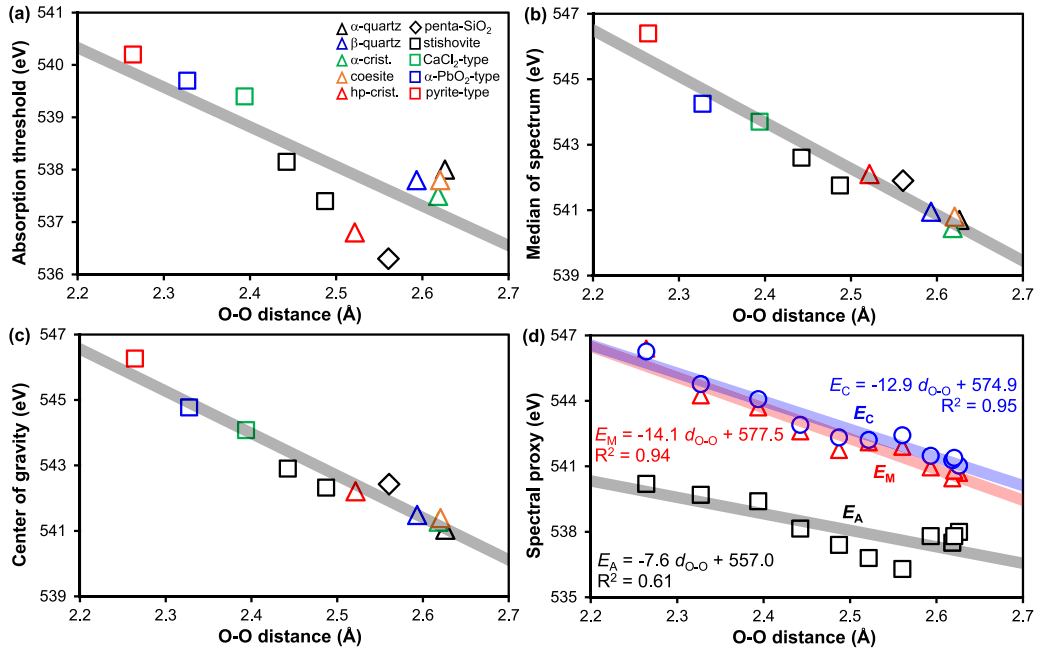


FIG. 7. Relationships among the absorption threshold (E_A), the median of spectrum (E_M), the edge energies at the center of gravity (E_C), and the average interatomic distances between nearest-neighboring O atoms (d_{O-O}) of the crystalline SiO_2 polymorphs as labeled: (a) E_A vs d_{O-O} , (b) E_M vs d_{O-O} , and (c) E_C vs d_{O-O} . (d) Correlations among each spectral proxy (E_A , E_M , and E_C) and d_{O-O} to compare the trend for each dataset. The black, blue, and red lines refer to the trends for E_C (circles), E_M (triangles), and E_A (squares), respectively.

feature has been attributed to the significant decrease in d_{O-O} accompanied by the formation of oxygen quadclusters [29]. Current results for the pyrite-type structure at ~ 271 GPa characterized are partly consistent with the earlier proposal where a reduction of d_{O-O} results in the formation of such higher-energy features at 548 eV.

D. Comparison of various spectral proxies for densification in crystalline and amorphous oxide under extreme compression: A view from O K -edge XRS

Based on the current simulations and previous theoretical results with characteristic evolution of the XRS patterns [27–30], several oxygen site-specific spectral proxies for oxide densification can be proposed and compared. Figure 7 presents the correlations for E_A , E_M , and E_C with the d_{O-O} of the SiO_2 phases. While the absorption energy threshold E_A of the O K -edge XRS spectrum has been useful to describe oxide densification, in Fig. 7(a), E_A and d_{O-O} in these SiO_2 phases beyond multimegabars are only moderately correlated [i.e., $E_A = -7.6 \times d_{O-O} + 557.0$ ($R^2 = 0.61$)]. Our previous study for the crystalline MgSiO_3 polymorphs showed a similar result between E_A and d_{O-O} in that E_A increases with decreasing d_{O-O} [i.e., $E_A = -10.5 \times d_{O-O} + 561.9$ ($R^2 = 0.7$)] [27]. The slight difference in the trend lines for the SiO_2 and MgSiO_3 polymorphs can be attributed to the effect of Mg on the densification mechanisms (see additional details below). The E_A factors in the pressure-induced shifts in the XRS spectra, mainly due to increase in E_G for oxides under pressure [27]. Despite the utility at relatively low-pressure conditions, the pressure-induced changes in E_A alone may not fully describe the observed pressure-induced spectral changes at the high-energy ranges (e.g., emergence of bimodal features

or convolution of the XRS features) for oxide beyond multi-megabar pressures.

Given the limitations of the E_A , alternative spectral proxies to better describe the observed XRS pattern are necessary. As introduced in our recent study, the center of gravity of the XRS spectra (E_C) [29] may describe the spectral evolution during compression. Furthermore, here, we also analyzed the energy at the median (E_M) of the calculated XRS features. While the E_C and E_M are expected to be similar, the difference may become prevalent when the XRS features deviate from the single monotonous pattern, which is often the case for spectra for the oxide under extreme compression (see Sec. 7 of the SM and Fig. S7 [50]; see also Refs. [29,30] therein). Figure 7 shows the evolution of the E_C and E_M with varying oxygen proximity. The *ab initio* simulations reveal intriguingly simple trends; the E_C and E_M decrease linearly with increasing d_{O-O} [$E_M = -14.1 \times d_{O-O} + 577.5$ ($R^2 = 0.94$) and $E_C = -12.9 \times d_{O-O} + 574.9$ ($R^2 = 0.95$); Figs. 7(b) and 7(c)]. The E_M and E_C follow similar trends, where the slight difference in trend lines arises from the differing statistical natures of “average (center of gravity)” and “median.” The difference between E_M and E_C may increase for the bimodal XRS features (Fig. S7). Both E_M and E_C provide useful spectral proxies for the structural densification of SiO_2 polymorphs, as shown by the improved R^2 values over those of E_A . Finally, E_M and E_C do not show strong correlations with $d_{\text{Si-O}}$ or Si coordination numbers in oxide phases (see Sec. 8 of the SM and Fig. S8 [50]). The E_G is also moderately correlated with E_A and E_C (see Sec. 9 of the SM and Fig. S9 for the detailed correlations of E_G vs E_A and E_G vs E_C [50]).

Because the d_{O-O} decreases linearly with increasing oxide bulk density (see Sec. 10 of the SM and Fig. S10 [50]), the observed trends in the E_M and E_C with d_{O-O} could be

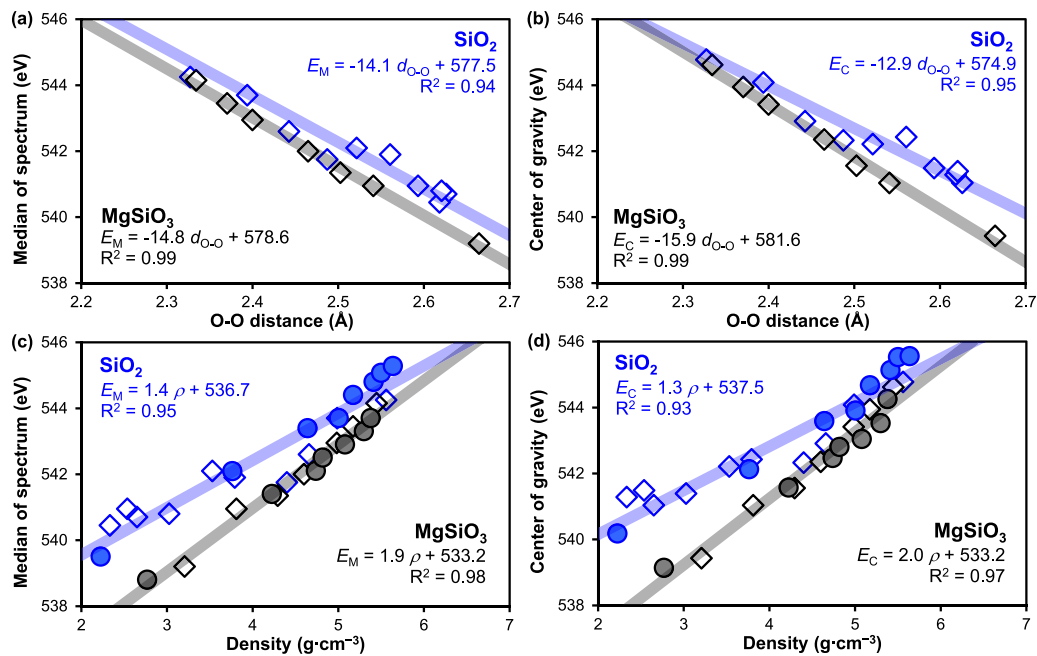


FIG. 8. Relationships among the median of spectrum (E_M), the edge energies at the center of gravity (E_C), and the average interatomic distances between nearest-neighboring O atoms (d_{O-O}) for crystalline SiO_2 and MgSiO_3 high-pressure polymorphs as labeled: (a) E_M vs d_{O-O} and (b) E_C vs d_{O-O} . Relationships among E_M , E_C , and the densities (ρ) for SiO_2 and MgSiO_3 crystals (empty) and glasses (filled) under high pressures as labeled: (c) E_M vs ρ and (d) E_C vs ρ . The black and blue lines refer to the trends for SiO_2 and MgSiO_3 , respectively. Data of crystalline MgSiO_3 polymorphs (from *ab initio* calculations) [27] and SiO_2 and MgSiO_3 glasses [from *in situ* high-pressure x-ray Raman scattering (XRS) experiments] [29,30] were retrieved from our earlier studies.

used as proxies for the oxide densification. As the effect of pressure on the XRS features has also been demonstrated for glassy and crystalline MgSiO_3 phases [27,28], the spectral proxies for both SiO_2 and MgSiO_3 phases under compression are discussed here. Figure 8 presents the relationships between E_C and E_M with varying d_{O-O} and ρ of the crystalline and noncrystalline SiO_2 and MgSiO_3 at high pressures [27,29,30]. In Fig. 8(a), the E_M of crystalline SiO_2 and MgSiO_3 polymorphs both decrease linearly with increasing d_{O-O} [$E_M = -14.1 \times d_{O-O} + 577.5 (R^2 = 0.94)$ for SiO_2 crystals and $E_M = -14.8 \times d_{O-O} + 578.6 (R^2 = 0.99)$ for MgSiO_3 crystals]. The E_C of SiO_2 and MgSiO_3 polymorphs in Fig. 8(b) also decrease linearly with increasing d_{O-O} , while the trend lines and R^2 values differ slightly from E_M [$E_C = -12.9 \times d_{O-O} + 574.9 (R^2 = 0.95)$ for SiO_2 crystals and $E_C = -15.9 \times d_{O-O} + 581.6 (R^2 = 0.99)$ for MgSiO_3 crystals]. Figures 8(c) and 8(d) demonstrate that the E_M and E_C for SiO_2 and MgSiO_3 increase linearly with increasing bulk density ρ . The E_M and E_C for SiO_2 and MgSiO_3 glasses from our earlier *in situ* XRS results are also shown [29,30]. While the dispersion increases with pressure, the overall trends are similar, showing linear increases in the E_M and E_C with ρ for both crystalline and noncrystalline oxides [$E_M = 1.4 \times \rho + 536.7 (R^2 = 0.95)$ for SiO_2 and $E_M = 1.9 \times \rho + 533.2 (R^2 = 0.98)$ for MgSiO_3 ; $E_C = 1.3 \times \rho + 537.5 (R^2 = 0.93)$ for SiO_2 and $E_C = 2.0 \times \rho + 533.2 (R^2 = 0.97)$ for MgSiO_3] (see Sec. 11 of the SM and Fig. S11 for the relationship between E_M and E_C [50]; see also Refs. [27,29,30] therein). The trends confirm that the E_M and E_C can also be effective spectral proxies for the densi-

fication of noncrystalline oxides under extreme compression, whereas how the d_{O-O} contractions are achieved in the oxide glasses may somewhat differ from those in the oxide crystals because of inherent differences in the medium- to long-range topologies [29,30].

Figure 9 presents a comparison of the O *K*-edge XRS spectra for α - PbO_2 -type SiO_2 (120 GPa) and MgSiO_3 bridgmanite (120 GPa) calculated via *ab initio* simulations [27] with the XRS patterns of SiO_2 and MgSiO_3 glasses collected experimentally under similar pressure conditions as in our previous studies [29,30]. The calculated XRS features for SiO_2 and MgSiO_3 high-pressure polymorphs are comparable with those for oxide glasses, as the emergence of high-energy features and the electronic delocalization indicate the formation of dense oxygen clusters with contractions in the d_{O-O} . Similarities in the XRS features indicate that the extent of d_{O-O} contractions in oxide glasses are comparable with those in oxide crystals, while the densification mechanisms for achieving the oxygen proximity may differ [29,30,66,67]. Furthermore, the densification mechanisms for fully polymerized SiO_2 and depolymerized MgSiO_3 differ. Therefore, the slopes in the $E_M(\rho)$ and $E_C(\rho)$ depend on the degree of network polymerization [68,69], accounting for the differences in the trend lines for SiO_2 and MgSiO_3 . Decreases in the Mg-O distances can also contribute to the densification of MgSiO_3 [30,67,70], while increases in the hybridization between O and Mg affect the spectral changes in the XRS spectra for MgSiO_3 at high pressures. In the complex silicate melts with multiple network modifiers (e.g., Ca, Na, Fe^{2+}), the $E_M(\rho)$ and $E_C(\rho)$ may be complicated further. We also acknowledge that both E_M and

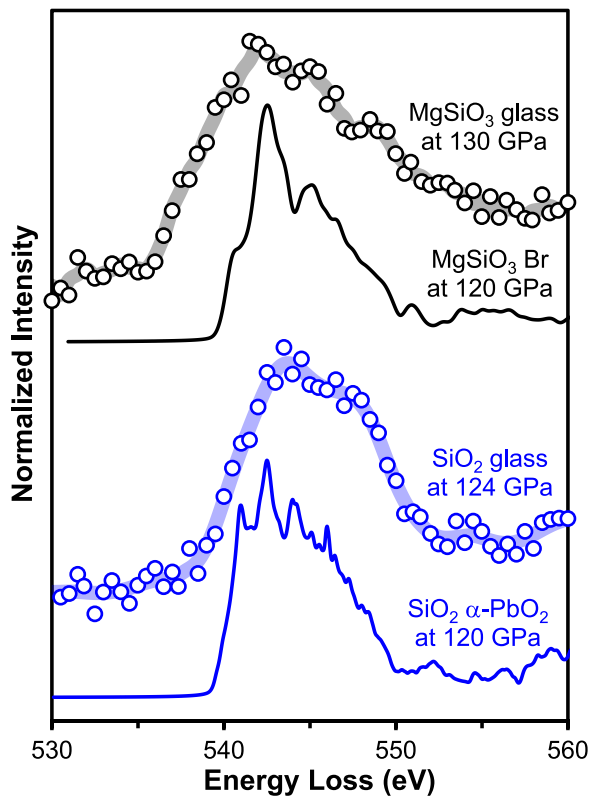


FIG. 9. Calculated O K -edge x-ray Raman scattering (XRS) spectra for α - PbO_2 -type SiO_2 at 120 GPa (blue) and MgSiO_3 bridgmanite at ~ 120 GPa (black). Experimental O K -edge XRS spectra of SiO_2 (blue) and MgSiO_3 (black) glasses under similar pressure conditions are shown for comparison. The XRS spectra for MgSiO_3 bridgmanite at ~ 120 GPa (from *ab initio* calculations) [27] and SiO_2 and MgSiO_3 glasses (from *in situ* high-pressure XRS experiments) [29,30] were retrieved from our earlier studies.

E_C may show nonlinear density (or $d_{\text{O-O}}$) dependence with finer pressure scans and/or under much higher-pressure conditions. Nevertheless, the observed trends for both SiO_2 and MgSiO_3 polymorphs with increasing pressures up to ~ 271 GPa present linear relationships among spectral proxies (E_M and E_C), $d_{\text{O-O}}$, and ρ from 1 atm to 270 GPa. Such linear correlations are expected to prevail for simple oxide systems. Although future confirmation is necessary, the trend can also highlight the potential application of XRS to diverse crystalline and amorphous silicates and the corresponding melts [29,30,71–73].

Current XRS studies, together with earlier experimental and theoretical studies [29,30] revealed a direct correlation between the density and the E_C and E_M for SiO_2 and MgSiO_3 glasses. Estimation of such parameters from experimental XRS spectra is often subject to some degree of uncertainty. For instance, XRS measurement involves multiple scattering processes, which contribute to the background of the XRS spectra [20,26]. The E_C (also E_M) values depend on how the backgrounds are subtracted [29]. Furthermore, limited spectral resolution of the XRS spectrometer at high incident x-ray energies (~ 1.4 eV full width at half maximum) may convolute minor features and lead to uncertainty in the parameters [36]. Finally, pressure gradients in the sample chamber and a range

of scattering vectors (q) may also contribute to uncertainty in the spectral parameters at high pressures [20,36]. *Ab initio* calculations provide direct information on the nature of chemical bonding without such artifacts and uncertainty, so estimated parameters from calculated XRS spectra can establish clear atomistic origins of the pressure-induced changes in the electronic structures [27]. Nevertheless, we found that the widths of the XRS features for crystals obtained from *ab initio* calculations depend somewhat on the calculation conditions. The high-energy features are, overall, underestimated—see Ref. [27] for details—resulting in a slightly narrower XRS spectrum. These limitations may lead to uncertainty in the E_C and E_M , but the direct comparison with the experimental XRS spectra for SiO_2 crystals may reconcile these issues.

Furthermore, because *ab initio* calculations do not directly provide the absolute energy values for the calculated O K -edge spectra, energy scales relative to the Fermi energy ($E - E_F$) need to be shifted to find a good match with experimental XRS spectra; while a precise determination of such a shift is not straightforward, we used the E_C values for α -quartz from experimental XRS spectra to calibrate the E_F . Note that the uncertainty in the E_F calibration may give rise to the systematic errors in the E_C and E_M (Fig. 8). The detailed methods for E_F shifts should be further reconciled [29,30]. Calculation of the electron binding energy is often necessary to properly align core-level excitation spectra for distinct target elements (such as oxygen in this paper). In our earlier studies, we have observed remarkable similarities between the experimental XRS data for crystalline and noncrystalline oxides and our calculated XRS spectra [27–30]. Thus, the further adjustment via theoretical calculations may not be necessary (see Sec. 4 of the SM for details [50]; see also Refs. [27–30,62] therein). Nevertheless, ongoing study could reveal the detailed electron binding energy and the potential core-level shift for distinct oxygen sites under extreme compression, particularly beyond multimegabar pressure conditions. Despite these uncertainties, current results demonstrate that, in addition to the qualitative interpretation of the XRS features (e.g., emergence of bimodal features), quantitative statistical analysis with E_C and E_M provides a novel structural proxy for the oxides under extreme pressure conditions.

IV. CONCLUSIONS

Calculated O K -edge XRS spectra of the crystalline SiO_2 phases, from α -quartz (1 atm) to the pyrite-type structure (271 GPa), enabled us to unveil how the oxygen-specific electronic bonding structures evolve upon crystal densification at multimegabar ranges, beyond the current experimental limits (~ 160 GPa), where the increases in the oxygen-proximity ($d_{\text{O-O}}$) via changes in the medium- to long-range periodicity control the extent of structural densification in crystals. Pressure-induced increase in electron interactions give rise to the emergence of characteristic doubletlike XRS features upon densification with decreasing $d_{\text{O-O}} < \sim 2.5$ Å. Merging of the bimodal features is also characteristic of the case where the $d_{\text{O-O}}$ becomes $< \sim 2.3$ – 2.4 Å. Significant electron delocalization in O $2p^*$ PDOS in the pyrite-type phase at ~ 271 GPa results from a reduced $d_{\text{O-O}} < \sim 2.2$ Å, leading to

the emergence of the high-energy feature at ~ 548 eV. The results suggest the key role of oxygen rearrangements in controlling the bulk densities in oxides under extreme pressure conditions. While we proposed the E_A of the O K -edge XRS spectrum as a representative of structural densification upon compression, E_C and E_M can be more reliable spectral proxies with which to quantify the pressure-induced changes in the overall XRS patterns. Despite the distinct crystal structures, the E_C and E_M for SiO_2 and MgSiO_3 (fully polymerized network vs depolymerized chain silicate) exhibit similar linear trends in the E_C and E_M vs $d_{\text{O-O}}$, indicating the governing role of oxygen proximity ($d_{\text{O-O}}$) in the oxygen-specific electronic structures for crystalline oxides at high pressure. Current results provide a predictive model with spectral proxies for the extent of structural densification in oxides under

extreme compression. Combining *in situ* high-pressure XRS experiments for oxides with site-resolved XRS calculations for well-known crystalline analogs can be a guide to understanding the electronic origins of the core-level excitation spectra of various crystalline and noncrystalline oxides under multimegabar pressures relevant to Earth and planetary deep interiors [73,74].

ACKNOWLEDGMENTS

We thank the anonymous reviewer for constructive suggestions which improved the quality of the manuscript. This paper was supported by the leader grant from the National Research Foundation of Korea (NRF; No. 2020R1A3B2079815) to S.K.L.

-
- [1] P. J. Tackley, in *Treatise on Geophysics*, 2nd ed., edited by G. Schubert (Elsevier, Oxford, 2015), p. 521.
- [2] T. Irifune and T. Tsuchiya, in *Treatise on Geophysics*, 2nd ed., edited by G. Schubert (Elsevier, Oxford, 2015), p. 33.
- [3] L. W. Finger and R. M. Hazen, *Rev. Mineral. Geochem.* **41**, 123 (2000).
- [4] K. Hirose, G. Morard, R. Sinmyo, K. Umemoto, J. Hernlund, G. Helffrich, and S. Labrosse, *Nature* **543**, 99 (2017).
- [5] F. González-Cataldo, S. Davis, and G. Gutiérrez, *Sci. Rep.* **6**, 26537 (2016).
- [6] M. Murakami, K. Hirose, S. Ono, and Y. Ohishi, *Geophys. Res. Lett.* **30**, 1207 (2003).
- [7] D. Andrault, G. Pesce, M. A. Bouhifd, B. N. Casanova, J. M. Hénot, and M. Mezouar, *Science* **344**, 892 (2014).
- [8] M. Murakami and J. D. Bass, *Phys. Rev. Lett.* **104**, 025504 (2010).
- [9] L. Stixrude, in *Treatise on Geophysics*, 2nd ed., edited by G. Schubert (Elsevier, Oxford, 2015), p. 417.
- [10] R. J. Angel, C. S. J. Shaw, and G. V. Gibbs, *Phys. Chem. Miner.* **30**, 167 (2003).
- [11] T. Yamanaka, T. Fukuda, Y. Komatsu, and H. Sumiya, *J. Phys.: Condens. Matter* **14**, 10545 (2002).
- [12] P. Cordier, D. Mainprice, and J. L. Mosenfelder, *Eur. J. Mineral.* **16**, 387 (2004).
- [13] B. B. Karki, M. C. Warren, L. Stixrude, G. J. Ackland, and J. Crain, *Phys. Rev. B* **55**, 3465 (1997).
- [14] K. J. Kingma, R. E. Cohen, R. J. Hemley, and H. K. Mao, *Nature* **374**, 243 (1995).
- [15] R. E. Cohen, *High Pressure Res.* **67**, 425 (1992).
- [16] T. Tsuchiya, R. Caracas, and J. Tsuchiya, *Geophys. Res. Lett.* **31**, L11610 (2004).
- [17] Y. Kuwayama, K. Hirose, N. Sata, and Y. Ohishi, *Science* **309**, 923 (2005).
- [18] T. Tsuchiya and J. Tsuchiya, *Proc. Natl Acad. Sci. USA* **108**, 1252 (2011).
- [19] J.-P. Rueff and A. Shukla, *Rev. Mod. Phys.* **82**, 847 (2010).
- [20] S. K. Lee, P. J. Eng, and H.-K. Mao, *Rev. Mineral. Geochem.* **78**, 139 (2014).
- [21] T. T. Fister, K. P. Nagle, F. D. Vila, G. T. Seidler, C. Hamner, J. O. Cross, and J. J. Rehr, *Phys. Rev. B* **79**, 174117 (2009).
- [22] N. Hiraoka and Y. Q. Cai, *Synchrotron Radiat. News* **23**, 26 (2010).
- [23] Y. Q. Cai, H. K. Mao, P. C. Chow, J. S. Tse, Y. Ma, S. Patchkovskii, J. F. Shu, V. Struzhkin, R. J. Hemley, H. Ishii, C. C. Chen, I. Jarrige, C. T. Chen, S. R. Shieh, E. P. Huang, and C. C. Kao, *Phys. Rev. Lett.* **94**, 025502 (2005).
- [24] Y. Meng, P. J. Eng, S. T. John, D. M. Shaw, M. Y. Hu, J. Shu, S. A. Gramsch, C. C. Kao, R. J. Hemley, and H. K. Mao, *Proc. Natl Acad. Sci. USA* **105**, 11640 (2008).
- [25] H. Fukui, L. T. Anh, M. Wada, N. Hiraoka, T. Iitaka, N. Hirao, Y. Akahama, and T. Irifune, *Proc. Natl Acad. Sci. USA* **116**, 21385 (2019).
- [26] C. Sternemann and M. Wilke, *High Pressure Res.* **36**, 275 (2016).
- [27] Y. S. Yi and S. K. Lee, *Phys. Rev. B* **94**, 094110 (2016).
- [28] Y. S. Yi and S. K. Lee, *Am. Mineral.* **97**, 897 (2012).
- [29] S. K. Lee, Y.-H. Kim, Y. S. Yi, P. Chow, Y. Xiao, C. Ji, and G. Shen, *Phys. Rev. Lett.* **123**, 235701 (2019).
- [30] Y.-H. Kim, Y. S. Yi, H.-I. Kim, P. Chow, Y. Xiao, G. Shen, and S. K. Lee, *Geophys. Res. Lett.* **46**, 13756 (2019).
- [31] S. K. Lee, J. F. Lin, Y. Q. Cai, N. Hiraoka, P. J. Eng, T. Okuchi, H. K. Mao, Y. Meng, M. Y. Hu, P. Chow, J. F. Shu, B. S. Li, H. Fukui, B. H. Lee, H. N. Kim, and C. S. Yoo, *Proc. Natl Acad. Sci. USA* **105**, 7925 (2008).
- [32] S. K. Lee, P. J. Eng, H.-K. Mao, and J. Shu, *Phys. Rev. B* **78**, 214203 (2008).
- [33] S. K. Lee, P. J. Eng, H.-K. Mao, Y. Meng, and J. Shu, *Phys. Rev. Lett.* **98**, 105502 (2007).
- [34] G. Lelong, G. Radtke, L. Cormier, H. Bricha, J. P. Rueff, J. M. Ablett, D. Cabaret, F. Gelebart, and A. Shukla, *Inorg. Chem.* **53**, 10903 (2014).
- [35] G. Lelong, L. Cormier, G. Ferlat, V. Giordano, G. S. Henderson, A. Shukla, and G. Calas, *Phys. Rev. B* **85**, 134202 (2012).
- [36] S. K. Lee, Y.-H. Kim, P. Chow, Y. Xiao, C. Ji, and G. Shen, *Proc. Natl Acad. Sci. USA* **115**, 5855 (2018).
- [37] S. Petitgirard, C. J. Sahle, C. Weis, K. Gilmore, G. Spiekermann, J. S. Tse, M. Wilke, C. Cavallari, V. Cerantola, and C. Sternemann, *Geochem. Perspect. Lett.* **9**, 32 (2019).
- [38] S. K. Lee, P. J. Eng, H.-k. Mao, Y. Meng, M. Newville, M. Y. Hu, and J. Shu, *Nat. Mater.* **4**, 851 (2005).
- [39] J. F. Lin, H. Fukui, D. Prendergast, T. Okuchi, Y. Q. Cai, N. Hiraoka, C. S. Yoo, A. Trave, P. Eng, M. Y. Hu, and P. Chow, *Phys. Rev. B* **75**, 012201 (2007).

- [40] S. K. Lee, S. Y. Park, H.-I. Kim, O. Tschauer, P. Asimow, L. Bai, Y. Xiao, and P. Chow, *Geophys. Res. Lett.* **39**, L05306 (2012).
- [41] B. J. A. Moulton, G. S. Henderson, H. Fukui, N. Hiraoka, D. de Ligny, C. Sonnevile, and M. Kanzaki, *Geochim. Cosmochim. Acta* **178**, 41 (2016).
- [42] N. Hiraoka, H. Fukui, and T. Okuchi, *High Pressure Res.* **36**, 250 (2016).
- [43] P. Chow, Y. M. Xiao, E. Rod, L. G. Bai, G. Y. Shen, S. Sinogeikin, N. Gao, Y. Ding, and H. K. Mao, *Rev. Sci. Instrum.* **86**, 072203 (2015).
- [44] M. Hou, Y. He, B. G. Jang, S. Sun, Y. Zhuang, L. Deng, R. Tang, J. Chen, F. Ke, Y. Meng, V. B. Prakapenka, B. Chen, J. H. Shim, J. Liu, D. Y. Kim, Q. Hu, C. J. Pickard, R. J. Needs, and H.-K. Mao, *Nat. Geosci.* **14**, 174 (2021).
- [45] C. Hébert, *Micron* **38**, 12 (2007).
- [46] Y. S. Yi and S. K. Lee, *Korean J. Mineral. Petrol.* **27**, 1 (2014).
- [47] H. Fukui, M. Kanzaki, N. Hiraoka, and Y. Q. Cai, *Phys. Chem. Miner.* **36**, 171 (2009).
- [48] H. Fukui, M. Kanzaki, N. Hiraoka, and Y. Q. Cai, *Phys. Rev. B* **78**, 012203 (2008).
- [49] M. Wu, Y. Liang, J.-Z. Jiang, and J. S. Tse, *Sci. Rep.* **2**, 398 (2012).
- [50] See Supplemental Material at <http://link.aps.org/supplemental/10.1103/PhysRevB.103.214109>, for the additional details on the computational methods for O *K*-edge XRS spectra calculations, estimations of E_A , E_M , and E_C of the O *K*-edge XRS spectra, and others, which includes Refs. [27–31,39,45,49,62,75,76].
- [51] G. Will, M. Bellotto, W. Parrish, and M. Hart, *J. Appl. Cryst.* **21**, 182 (1988).
- [52] K. Kihara, *Eur. J. Mineral.* **2**, 63 (1990).
- [53] W. W. Schmahl, I. P. Swainson, M. T. Dove, and A. Graeme-Barber, *Z. Kristallogr.* **201**, 125 (1992).
- [54] L. Huang, M. Durandurdu, and J. Kieffer, *Nat. Mater.* **5**, 977 (2006).
- [55] J. Badro, D. M. Teter, R. T. Downs, P. Gillet, R. J. Hemley, and J.-L. Barrat, *Phys. Rev. B* **56**, 5797 (1997).
- [56] D. Andraut, G. Fiquet, F. Guyot, and M. Hanfland, *Science* **282**, 720 (1998).
- [57] D. M. Teter, R. J. Hemley, G. Kresse, and J. Hafner, *Phys. Rev. Lett.* **80**, 2145 (1998).
- [58] K. Momma and F. Izumi, *J. Appl. Cryst.* **44**, 1272 (2011).
- [59] P. Blaha, K. Schwarz, G. Madsen, D. Kvasnicka, and J. Luitz, *WIEN2k* (Technische Universität Wien, Vienna, 2001).
- [60] J. P. Perdew, A. Ruzsinszky, G. I. Csonka, O. A. Vydrov, G. E. Scuseria, L. A. Constantin, X. Zhou, and K. Burke, *Phys. Rev. Lett.* **100**, 136406 (2008).
- [61] K. Schwarz, *J. Solid State Chem.* **176**, 319 (2003).
- [62] P. Blaha, K. Schwarz, F. Tran, R. Laskowski, G. K. H. Madsen, and L. D. Marks, *J. Chem. Phys.* **152**, 074101 (2020).
- [63] E. de Clermont Gallerande, D. Cabaret, G. Lelong, C. Brouder, M. B. Attaiaa, L. Paulatto, K. Gilmore, C. J. Sahle, and G. Radtke, *Phys. Rev. B* **98**, 214104 (2018).
- [64] A. R. Oganov, M. J. Gillan, and G. D. Price, *Phys. Rev. B* **71**, 064104 (2005).
- [65] H. Fujihisa, Y. Akahama, H. Kawamura, Y. Ohishi, O. Shimomura, H. Yamawaki, M. Sakashita, Y. Gotoh, S. Takeya, and K. Honda, *Phys. Rev. Lett.* **97**, 085503 (2006).
- [66] M. Murakami and J. D. Bass, *Proc. Natl Acad. Sci. USA* **108**, 17286 (2011).
- [67] D. B. Ghosh, B. B. Karki, and L. Stixrude, *Am. Mineral.* **99**, 1304 (2014).
- [68] S. K. Lee, B. O. Mysen, and G. D. Cody, *Phys. Rev. B* **68**, 214206 (2003).
- [69] B. Mysen and P. Richet, in *Silicate Glasses and Melts*, 2nd ed., edited by B. Mysen and P. Richet (Elsevier, Amsterdam, 2019), p. 109.
- [70] L. Stixrude and B. Karki, *Science* **310**, 297 (2005).
- [71] T. Sato and N. Funamori, *Phys. Rev. Lett.* **101**, 255502 (2008).
- [72] S. Petitgirard, W. J. Malfait, B. Journaux, I. E. Collings, E. S. Jennings, I. Blanchard, I. Kantor, A. Kurnosov, M. Cotte, T. Dane, M. Burghammer, and D. C. Rubie, *Phys. Rev. Lett.* **119**, 215701 (2017).
- [73] S. K. Lee, J. L. Mosenfelder, S. Y. Park, A. C. Lee, and P. D. Asimow, *Proc. Natl Acad. Sci. USA* **117**, 21938 (2020).
- [74] Y. Kono, Y. Shu, C. Kenney-Benson, Y. Wang, and G. Shen, *Phys. Rev. Lett.* **125**, 205701 (2020).
- [75] S. J. Clark, M. D. Segall, C. J. Pickard, P. J. Hasnip, M. J. Probert, K. Refson, and M. C. Payne, *Z. Kristallogr.* **220**, 567 (2005).
- [76] J. P. Perdew, K. Burke, and M. Ernzerhof, *Phys. Rev. Lett.* **77**, 3865 (1996).